Aqueous blackbody calibration source for millimeter-wave/terahertz metrology

Charles Dietlein,[1,2,*] Zoya Popović,[1] and Erich N. Grossman[2]

[1]Department of Electrical and Computer Engineering, University of Colorado at Boulder, Boulder, Colorado 80309-0425, USA

[2]Optoelectronics Division, National Institute of Standards and Technology, 325 Broadway, Boulder, Colorado 80305-3328, USA

*Corresponding author: dietlein@boulder.nist.gov

Received 16 May 2008; accepted 25 June 2008;
posted 29 August 2008 (Doc. ID 96188); published 15 October 2008

This paper describes a calibrated broadband emitter for the millimeter-wave through terahertz frequency regime, called the aqueous blackbody calibration source. Due to its extremely high absorption, liquid water is chosen as the emitter on the basis of reciprocity. The water is constrained to a specific shape (an optical trap geometry) in an expanded polystyrene (EPS) container and maintained at a selected, uniform temperature. Uncertainty in the selected radiometric temperature due to the undesirable reflectance present at a water interface is minimized by the trap geometry, ensuring that radiation incident on the entrance aperture encounters a pair of s and a pair of p reflections at 45°. For water reflectance R_w of 40% at 45° in the the W-band, this implies a theoretical effective aperture emissivity of $(1 - R_{ws}^2 R_{wp}^2) > 98.8\%$. From the the W-band to 450 GHz, the maximum radiometric temperature uncertainty is ±0.40 K, independent of water temperature. Uncertainty from 450 GHz to 1 THz is increased due to EPS scattering and absorption, resulting in a maximum uncertainty of ~3 K at 1 THz.

OCIS codes: 120.3930, 120.3940, 120.4800, 120.5630.

1. Introduction

The techniques and infrastructure available for the metrology of radiometric power and related quantities in the millimeter-wave and terahertz frequency ranges are far less advanced than at optical and infrared frequencies. However, applications in this frequency range are rapidly emerging [1–3], and a metrological infrastructure in the form of standardized techniques and hardware would significantly benefit progress in many applications. One example is millimeter-wave remote sensing for atmospheric science, where the importance of accurate calibration and the shortcomings of present calibration targets are widely appreciated [4,5]. Another example is millimeter-wave/terahertz detector arrays for security applications, in which accurate measurement of noise-equivalent power and noise-equivalent temperature difference is essential in evaluating device performance. In most cases, noise-equivalent power or noise-equivalent temperature difference is the most important factor in determining the overall effectiveness of a security system. The blackbody calibration source described in this paper has been developed to solve this problem for a particular passive millimeter-wave detector program [6], but the resulting standard is generally applicable for calibration and measurement needs from 100 GHz to 1 THz.

In addition to numerous application-specific calibration sources and techniques for infrared radiometers such as in [7,8], the existing metrology infrastructure for optical and infrared radiometry is comprehensive, rigorous, and widely accepted [9–12]. Portions of it can be directly adapted to the millimeter-wave/terahertz frequency regime; e.g., high-temperature infrared blackbodies are key components in the traceability chain for infrared power measurements. The aqueous blackbody calibration source presented in this work, hereafter referred to as the "ABC source," represents an effort to bring similarly systematic and traceable measurement techniques to the millimeter-wave/terahertz frequency range.

The purpose of the ABC source is to emit into free space an absolutely calibrated power spectral

density (radiometric temperature) in the millimeter-wave to terahertz frequency regime. More specifically, the source enables

1. Accurate measurement of the responsivity and noise-equivalent temperature difference of detectors and detector arrays.
2. An absolutely calibrated source of power, when combined with an appropriate bandpass filter [13–15].
3. A scene simulator that generates an accurate radiometric temperature spatial profile when combined with an appropriate mask.
4. Ultrawideband frequency-response device measurements, since the ABC source emissivity has a well known frequency dependence.

A blackbody source must be highly absorptive, and its physical temperature must be accurately known. We note that the Rayleigh–Jeans approximation to Planck's law of blackbody radiation is utilized in this frequency range throughout this paper, that is, spectral radiance is proportional to temperature: $I(f,T) = 2k_B T f^2/c^2 (\mathrm{W} \cdot \mathrm{sr}^{-1} \cdot \mathrm{Hz}^{-1} \cdot \mathrm{m}^{-2})$. The most common blackbody source for this frequency range is millimeter-wave anechoic foam soaked in liquid nitrogen ($T = 77\,\mathrm{K}$). Although such foams are relatively good absorbers, and more sophisticated anechoic materials with even lower reflectance exist [16], the foam rarely remains at $T = 77\,\mathrm{K}$ longer than 1 min when held in air. Even if left floating in the liquid (constraining the geometry to vertical beams), its radiometric temperature varies unpredictably. Formation of ice on the foam surface increases its reflectance, and moisture increases in the intervening atmosphere and condenses on all exposed surfaces. Heating such anechoic materials is an inadequate alternative because they are poor thermal conductors and therefore do not remain isothermal [5,17,18]. Infrared photographs of pyramidal foam panels show the tips of the pyramids closer to ambient temperature than are the pits between pyramids [19]. On the other hand, a well-mixed and easily heated fluid such as water provides an accurate physical temperature (one example that takes advantage of this is an IR blackbody source utilizing water for temperature control [20]). Moreover, water is extremely lossy at these frequencies, implying high emissivity. Unfortunately, the high dielectric constant of water dictates a high reflectance at a water–air interface, approximately $R_w = 30\%$ in the the W-band at normal incidence. This makes the radiometric temperature of a simple water bath highly dependent on the uncontrolled temperature of the ambient surroundings.

The novelty of the ABC source is its operating frequency range. In the visible and infrared, many blackbody cavities contain deep grooves or pits with internal corners. The radius of curvature of these corners, and the characteristic size of surface roughness and other manufacturing features is usually comparable to or greater than the wavelength. In the terahertz range, however, the ratio of wavelength to radius of curvature is much larger, and the capabilities and tolerances available from molded expanded polystyrene are completely different than for optical blackbody materials, demanding a new set of cavity geometry constraints. Additionally, material properties in this frequency range are much less well known than at either microwave or infrared/optical frequencies. Given the variety of corrections and uncertainties that must be considered in design of an *absolutely calibrated* source, we chose to adopt a geometry in which all radiometrically active surfaces are planar—a geometry that lends itself to straightforward analysis.

The paper is organized as follows: Section 2 describes the optical trap principle of operation and nominal operating ranges, Section 3 presents the uncertainty analysis, Section 4 summarizes measurement results, and Appendix A contains the details of the uncertainty analysis. Important symbols are as follows: R (reflectance), T (temperature), and A (absorbance). The subscripts w, e, and m correspond to water, expanded polystyrene (EPS), and mirror, respectively. Additionally, the subscripts r and 0 are used to denote radiometric and ambient temperatures.

2. Principle of Operation

A. Optical Trap Design

An "optical trap" is a component designed in such a way that the power from consecutive specular reflections of incident light is collected and measured, with very little power evading measurement. The initial optical traps were developed by Zalewski and Duda [21], furthered by Fox [22] and Gardner [23] and advanced by Lehman and Cromer [24,25] in the design of absolute powermeters for fiber optics. The ABC source geometry can be viewed as a "terahertz trap," with the detector surfaces replaced by water. By reciprocity, it can be considered as either an emitter or an absorber of millimeter-wave/terahertz radiation. In the absorber modality, the surfaces that reflect and detect radiation in the optical trap geometry are replaced in the ABC source by highly absorbing water surfaces, defined by the shape of the "transparent" EPS water container. Given the reflectance of water (R_w) at an incidence angle of 45° of ≈40% at $f = 100\,\mathrm{GHz}$ [26], we impose the requirement of at least four reflections from water surfaces at this angle. This rough calculation provides the basis for the design, such that the effective emissivity at the aperture is $(1 - R_{ws}^2 R_{wp}^2)$ with ideal materials, or 98.8% at $f = 100\,\mathrm{GHz}$, and increases with frequency. Furthermore, the geometry is specified such that the ABC source is polarization insensitive; i.e., the number of water reflections is divided equally between s and p polarizations.

Initially, a simple geometry with two water surfaces and an ideal mirror, shown in Fig. 1, was

simulated using geometric optics. Rays initiating from the 20 cm square entrance aperture in the x-y plane are first incident on a water surface in the $\langle 1, 0, -1\rangle$ plane. Upon specular reflection from the first water surface, a second water surface in the $\langle -1, -1, 0\rangle$ plane is encountered and a second reflection occurs. The third reflection is from an ideal mirror in the $\langle 0, 1, 0\rangle$ plane, after which the geometric optics path is reversed and the rays exit the geometry in the opposite order.

An improved design, obtained by extending the two planes in $+z$ until converged, is shown in Fig. 2 as realized in a fully manufacturable EPS geometry. Two cavities in the EPS can be defined: one that contains the water, and one in which the entrance aperture is located. Beyond the EPS–water interfaces, the shape of the water cavity is irrelevant other than that its thickness must be great enough that transmittance through the water is negligible and that the water remains isothermal. In geometric terms, the cavity in which the entrance aperture is located is a prismatoidal pentahedron created by truncating an apex of a right isosceles tetrahedron; the parallel planes of the remaining pyramidal frustum form similar right isosceles triangles. These parallel planes form the top and bottom of the cavity. Two of the remaining lateral trapezoidal walls are the water surfaces. The remaining plane contains the aperture of the ABC source, defined by a square subtending the acute angle of the trapezoid. Due to manufacturing constraints, an additional 2.5 cm of distance separates the bottom of the cavity from the mirror; this does not adversely affect simulation or test results.

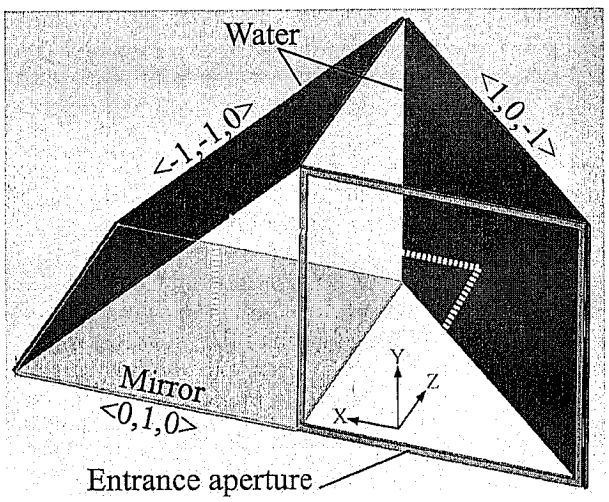

Fig. 1. (Color online) Trimetric view of the simplified ABC source geometry. The entrance aperture is defined by the square annulus in the $\langle 0, 0, 1\rangle$ plane, the darker planes ($\langle -1, -1, 0\rangle$ and $\langle 1, 0, -1\rangle$) represent water surfaces, and the light gray plane ($\langle 0, 1, 0\rangle$) corresponds to the ideal mirror. The ray indicated by the thick dashed line enters the center of the aperture normally and is incident on the center of each water surface and the mirror. Omitted for clarity is the return path following the same ray path, providing two more reflections from water surfaces before exiting the aperture.

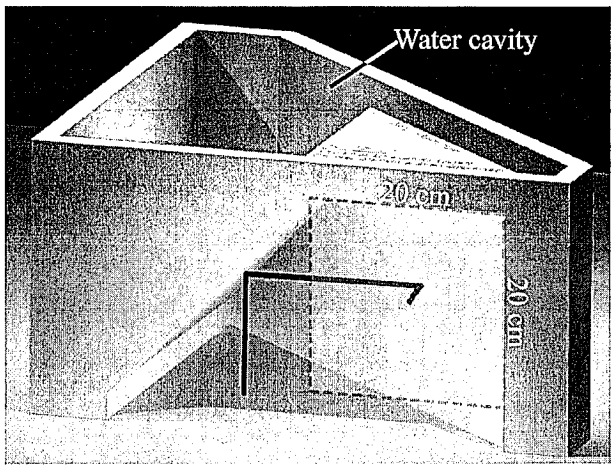

Fig. 2. (Color online) Trimetric rendering of the manufactured ABC source. The 20 cm × 20 cm entrance aperture is highlighted by the dashed square and translucent overlay, and the geometric path is indicated by the heavy solid lines. The mirror is omitted for clarity.

The thickness of the radiometrically relevant EPS–water interface walls of the ABC source is 1 cm. Excluding these two 45° walls, all other walls are drafted by 1° to enable removal of the mold during the fabrication process, and are 2.5 cm thick for structural stability. The overall footprint of the ABC source is 53 cm × 27 cm × 50 cm, and the water volume is 21 L when filled to within 2 cm of the top.

B. Nominal Operating Ranges

Actual radiometric temperature is a function of position in the plane of the entrance aperture, incidence angle, and frequency. Geometric optics is used to simulate the manufactured geometry described in the previous section. In general, the highest performance is found in the center of the entrance aperture for rays that are normal to the entrance aperture. In this context, performance is defined by the fraction of incident rays that are absorbed by a water surface; one minus this quantity is return loss. Figure 3 shows the results of geometric optics simulations, varying position and angle of the source in the entrance aperture. The frequency-dependent complex index of refraction, $\hat{n}(f) = n(f) - jk(f)$, from experimental data in [26] is applied to the water surfaces in the ray-tracing simulations, at $f \approx 200$ GHz (specifically, $\hat{n} = 2.73 - j1.37$). It is noted that the exact value of $\hat{n}(f)$ is model dependent, so there is a range of values for n at a specific frequency, especially in the range of $f = 50$ GHz–$f = 200$ GHz, where $\hat{n}$ changes rapidly. The simulation is performed by moving a small bundle of many rays along x and y in the entrance aperture, and at each xy position, varying θ_x or θ_y, and tracing all rays originating from the specific combination of position and orientation. Every ray path is recorded, and at each position and orientation, the total percentage of incident rays that terminate in a water surface is summed. It is seen that when

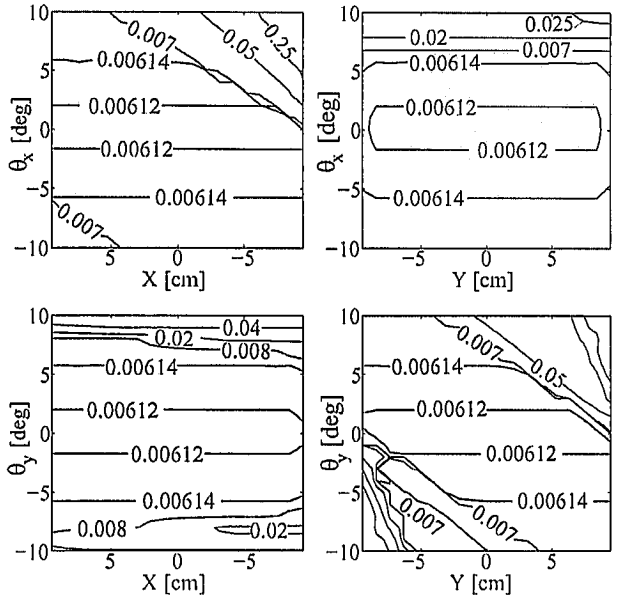

Fig. 3. Contour plots of performance for the manufactured geometry. Contour values are linear return loss, for $f = 200$ GHz, using the model parameters for water from [26]. Note that for the plots on the left, the coordinates of the abscissas are reversed from standard to match the notation shown in Fig. 1. Both plots on the right, where Y is the abscissa, can be rotated 90° counterclockwise to match Fig. 1. The contour values are *not* evenly spaced, due to rapidly changing values near the plot edges; additionally, the central region in each plot is shaded to illustrate locations and orientations of high performance, the "sweet spot."

incident ray orientation orthogonal to scan position (abscissas in Fig. 3) is varied, peak performance—represented by the shaded "sweet spot" in Fig. 3—is always maintained for $\theta \leq \pm 6°$ and position $\leq \pm 10$ cm. When varying orientation coplanar with scan position, performance degrades primarily when the detector is oriented in the same direction as the offset, that is, when it is pointed away from the center of the first water surface. At center, return loss remains at its best value over an angular range of $-6° < \theta < 6°$ for both θ_x and θ_y. At normal incidence, return loss remains at its best value over a spatial range of $-10\text{ cm} < x < 10\text{ cm}$ or $-10\text{ cm} < y < 10\text{ cm}$. When both position and orientation vary from centered and normal, respectively, incident rays no longer encounter four reflections from water at the desired incidence angle, and performance falls off, as shown in Fig. 3.

3. Radiometric Temperature Accuracy Analysis

Ideally, the actual radiometric temperature (T_r) of the ABC source is equal to the physical temperature of the water (T_w). In reality, the two differ slightly because of residual dependencies in T_r on ambient temperature (T_0), water temperature spatial nonuniformity, EPS loss (A_e), water reflectance (R_w), mirror absorbance (A_m), scattering, stray radiation, diffraction, deformation of the EPS walls, and atmospheric attenuation. All of these are frequency dependent, and in this section and Appendix A, we discuss these differences quantitatively. Measurement of T_r will have errors that can be classified as either correctable biases or uncertainties; furthermore, uncertainties in the corrections can be classified as either Type A or Type B [27]. Some of the above effects result in uncertainties in radiometric temperature that can be summarized in the uncertainty budget, which is presented in Table 2 below. The others do not affect the accuracy of T_r but instead restrict the range of frequency, area, or solid angle over which the uncertainty estimates remain accurate. We have not included them in the uncertainty budget, but they are summarized for completeness in Table 3 below.

A. Water Temperature Measurement Uncertainty

The most straightforward component of the uncertainty budget is the uncertainty in the measurement of T_w. In the particular implementation of the ABC source used for the measurements described in Section 4, a commercial immersion circulator was used to simultaneously mix and heat the water, and six platinum resistance thermometers were placed throughout the volume of the water to measure T_w. The maximum water temperature available from our circulator, which has a maximum power rating of 1100 W, is about 65 °C (333 K). The accuracy of the thermometers is described by DIN IEC 751, which specifies a Type B uncertainty of ±0.24 K for this temperature range [28]. This uncertainty is independent of water temperature and frequency.

B. Water Temperature Nonuniformity

Spatial nonuniformity of the water temperature throughout the water bath could increase the measurement uncertainty of the water temperature, despite use of the circulator. Therefore, the nonuniformity was measured for three cases with water circulated: while ramping up the water temperature at full heater power, while holding the water temperature constant, and while allowing the water to naturally cool to ambient temperature. In both the last two cases, the nonuniformity throughout the water volume, as indicated by the readings of the six thermometers, was less than their Type B uncertainty. In the first case, the water was isothermal to within the thermometer uncertainty, except for the water immediately behind the first/fourth water surface, where circulation was poorer. Under full heater power, the temperature lag for this region was approximately 1 K, and the time lag approximately 1 min. Therefore, as long as the ABC source is allowed to stabilize for at least 1 min before radiometric measurements are begun, the nonuniformity can be neglected and the total uncertainty due to water temperature measurement remains at the ±0.24 K Type B uncertainty of the thermometers.

C. EPS Loss

Since EPS is the lowest-loss solid material in the frequency range of interest, it has been the object

of considerable previous study [29]. For $f > 500$ GHz, its transmission properties depend on the specific sample under test. The parameters that affect EPS transmission are the initial (pre-expansion) polystyrene bead size, the final density of the expanded material, and thickness; these parameters *also* directly affect its mechanical strength. Transmittance is a stronger function of density than of bead size, but bead size greatly influences the seepage of water into the EPS. We chose the smallest commercially available polystyrene bead size ($d < 0.5$ mm) in order to minimize water leakage and reduce scattering loss (at a density of 96 g/L, this is the EPS material used in everyday containers for hot beverages). To maintain both structural integrity and high transmittance, a trade-off in density is made. For a thickness of 1 cm, 100 g/L EPS is opaque above $f =$ (500–1000) GHz but mechanically sturdy. On the other hand, 25 g/L EPS has greater than 50% transmission at $f = 2$ THz, but the wall is flexible and permeable to water. Thus, 55 g/L was chosen as a compromise.

The electromagnetic properties—transmittance, absorbance, and scattering—of EPS dominate the performance of the ABC source at high frequencies. That is, at high frequencies, the incident radiation not absorbed in water is primarily absorbed in or scattered by the EPS walls, which lie at a lower temperature than the water. Because of the sample dependence of EPS optical properties, our strategy was to measure the loss of the EPS actually used in the construction of the ABC source to estimate the EPS absorbance A_e. In our measurement, the one-way transmittance of EPS with the same density, bead size, and thickness as the manufactured ABC source was measured between $f = 75$ GHz and $f = 200$ GHz by use of a tunable Gunn oscillator and a commercial powermeter. In this range, transmission loss for a 1 cm thick sample is smaller than the upper limit of $A_e \approx 0.005$, which is set by the stability of the source and is therefore a Type A uncertainty. A Fourier-transform infrared (FT-IR) spectrometer is utilized at the low end of its operating range for measurements up to $f = 6$ THz; combined results from both measurements between $f = 75$ GHz and $f =$ 1.1 THz are shown in Fig. 4 (transmittance drops to zero by $f = 3$ THz for the specific EPS utilized in the ABC source).

The temperature profile of an EPS wall with T_w on one side and T_0 on the other side is a linear ramp from T_0 to T_w, so that the effective temperature T_e of the EPS is the mean temperature of the two. Thus, in passing through a single wall of EPS whose absorbance is A_e, the radiometric temperature T_r of the blackbody emission from the water is reduced by $\Delta T_r = A_e(T_0 + T_w)/2$ for $A_e \ll 1$. In Appendix A, this basic radiative transfer result is applied to the full ABC source geometry to obtain the effect of a nonzero A_e on the ABC source radiometric temperature.

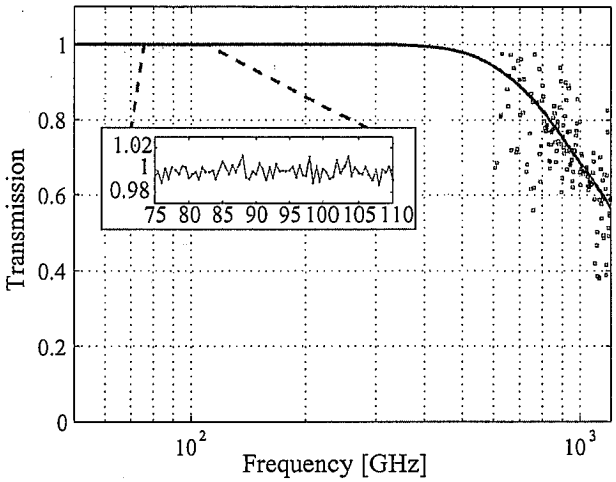

Fig. 4. (Color online) Transmission through 1 cm thick EPS at normal incidence. $f > 600$ GHz measured with an FT-IR spectrometer, and from $f = 75$ GHz to $f = 200$ GHz measured with a tunable Gunn diode and commercial powermeter. Combined data are smoothed by a moving-average filter with a 10% span and fit to $y = 1/2\{1 + \mathrm{erf}[(x-\mu)/(\sigma\sqrt{2})]\}$, and the region between $f =$ 200 GHz and $f = 600$ GHz is interpolated. The inset shows measured data in the W-band.

However, in our transmission measurements, as in those of Zhao *et al.* [29], true absorption in the EPS is not distinguished from scattering. The measured quantity is simply the reduction in power coupled from source to detector. In fact, scattering is thought to be the dominant loss mechanism. To the extent that our measurement of A_e reflects scattering and not absorption, the analysis in Appendix A will overestimate its impact on T_r. This is easily seen in the case of absorption (rather than emission) through a single EPS wall: incident radiation that is scattered in the EPS will still be absorbed in the water, just not in water directly behind the incident spot on the EPS surface. For the full ABC source, this implies that EPS scattering would not necessarily reduce the radiometric temperature below T_w within the specified $A\Omega$ of the source. However, the size of the "sweet spot" in position and orientation would diminish somewhat. If the balance between absorption and scattering were known, then the reduction in T_r due to absorption would be a calculable correction with Type A uncertainty, but because the balance is not known, we consider A_e to be a Type B uncertainty. In short, the effect of EPS loss is that above $f = 200$ GHz the radiometric temperature of the ABC source is not the water temperature, but rather a lower temperature, where the *worst-case* result (i.e., measured transmission loss is treated entirely as absorption) is calculable.

D. Water Reflectance

To obtain nonzero reflectance from a water boundary is the reason for adopting an optical trap geometry for a millimeter-wave/terahertz blackbody in the first place. The dielectric constant of liquid water follows

a double-Debye model [26] in the millimeter-wave/terahertz frequency regime. By use of this model, the Fresnel coefficients can be obtained for reflectance at 45° incidence from a water and EPS interface (assuming an EPS refractive index of $n_{EPS} \approx 1$ in the W-band). Impurities in water could decrease the performance of the ABC source, but the effect is thought to be very small [30]; all our tests have utilized plain tap water. The temperature of liquid water in this frequency range also modifies its dielectric constant [31]; when four water reflections are encountered, the resulting performance variation is minimal but existent. The result for water reflectance, R_w, at 45° is shown in Fig. 5 for both polarized and unpolarized radiation at two water temperatures. High reflectance increases radiometric error at low frequencies but is correctable; the total, four-bounce reflectance of the ABC source is a calculable correction. At $f = 100$ GHz, for example, and as demonstrated in Appendix A, the total reflectance is $\approx 0.7\%$ (return loss of −21 dB). The Type B uncertainty in this correction can be deduced from the uncertainty reported in four of the double-Debye model parameters by both [26,31], which we have propagated through Eq. (A1) for calculation of the radiometric error (including both corrections and uncertainties).

E. Mirror Reflectance

At millimeter-wave and terahertz frequencies, due to surface roughness and skin effect losses, unpolished metal sheets are not perfect mirrors. Reflectivity from a nonmagnetic imperfect conductor can be derived as

$$R_m \approx 1 - 2\sqrt{\frac{4\pi f \epsilon_0}{\sigma}}, \tag{1}$$

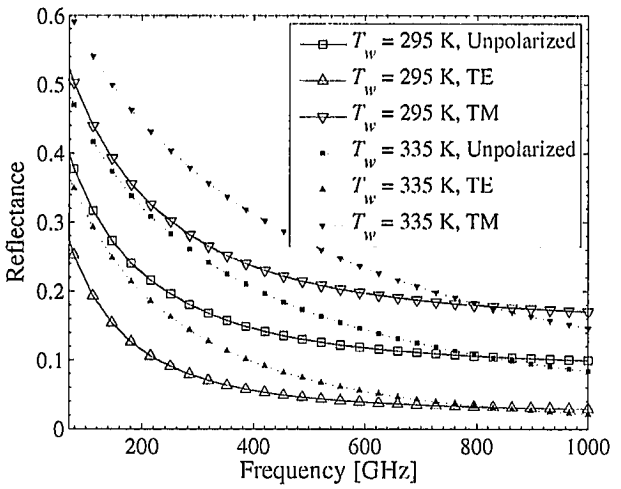

Fig. 5. Calculated water reflectance R_w at an incidence angle of 45° plotted through the frequency range of interest for polarized and unpolarized radiation at two physical temperatures.

where σ is conductivity. This approximation is valid for a good conductor, that is, when $(\sigma/\omega\epsilon)^2 \gg 1$. For the case of Al and normal incidence at $f = 100$ GHz, $R_m = 0.9989$. Realistic metal mirrors with finite roughness display lower reflectance, though when the rms roughness is small compared to λ, the primary effect is not absorption but low-angle scattering. Ohmic loss in the mirror, A_m, reduces the radiometric temperature of the source, since the physical temperature of the mirror is T_0, but low-angle scattering has much less effect since most of the light scattered into the $A\Omega$ described in Fig. 3 would come from water at T_w anyway. Because of the difficulty of knowing the true surface roughness of the mirror in the ABC source, and more importantly, the difficulty of estimating the relevant radiometric loss from the surface roughness, we simply assume a worst-case loss—a Type B uncertainty—of $A_m = 0.05$ for purposes of estimating the uncertainty in T_r. In Appendix A, the effect of nonzero A_m on the radiometric temperature is calculated in Eq. (A4).

F. Other Nonidealities

The primary effect of the remaining nonidealities is to reduce the area, solid angle, and/or frequency over which the ABC source maintains its desired radiometric temperature, that is, they do not affect T_r for normal-incidence measurements centered in the entrance aperture. These nonidealities include scattering from the surface of the water, diffraction at the entrance aperture, EPS wall deformation, and atmospheric attenuation.

The diameter of the polystyrene beads, postexpansion, is $d = (0.6–0.7)$ mm, but at the nominally flat surface of the EPS, the average feature size is approximately 0.1 mm. This corresponds to water surface features ranging in size from $\lambda/30$ to $\lambda/3$, implying that scattering needs to be considered. Scattering manifests itself as decreased specular reflectance and increased diffuse reflectance, gradually reducing the validity of the geometric optics simulations. Rays of unknown origin (temperature) and incidence angle outside the cone of acceptance are brought into the cone of acceptance via diffuse reflection and can thus be radiated out of the entrance aperture to a detector. The classic Rayleigh criterion describes the distinction between rough and smooth surfaces as far as phase coherence across a reflected wavefront is concerned. The boundary between "rough" and "smooth" is frequently described as an rms surface roughness of $\xi = \lambda/8$. A more rigorous treatment leads to the result that the ratio of specularly reflected radiation to total reflected radiation is $\Upsilon = \exp[-(4\pi\xi \cos\theta_i/\lambda)^2]$, where θ is the incidence angle [32]. Using a value for rms roughness of 15 μm based on the measured correlation length (expanded bead size) and peak roughness height (indentation between cells) of the EPS, Υ varies from 0.998 at $f = 100$ GHz to 0.969 at $f = 400$ GHz. Thus at $f = 400$ GHz, approximately 3% of the total reflected radiation is diffusely reflected from the water

according to a distribution function that is dependent upon its statistical surface profile. At this time, the reflectance distribution function is not known, absent a correct model of the water surface profile.

Due to the large bandwidth and electrical size of the ABC source, diffraction should be considered in a complete analysis. If a limiting aperture or defining baffle is introduced at the entrance aperture, diffraction loss will increase and should be calculated according to the exact geometry implemented. However, in most operating conditions, the emission from the ABC source will overfill the solid angle of the detector, with no limiting or defining aperture. The power lost to diffraction in the nonlimiting aperture case, assuming the detector is at the optimum position and orientation in the aperture, is calculated for the ABC source to be $0 \pm 0.2\%$ at the W-band, depending on the solid angle subtended by the detector and the formalism used [33,34]. When the detector is at a nonstandard position or orientation in the entrance aperture, or at a greater distance from the ABC source, diffraction loss must be recalculated accordingly.

Another nonideal condition stems from the compromise of choosing relatively thin and moderate-density EPS to enhance transmittance at the expense of mechanical strength. Because of the weight of the water on the second EPS–water interface, which is at a 45° angle from vertical, the surface deflects (becomes convex). A two-dimensional sketch of the resulting unfolded optical diagram is shown to scale in Fig. 6, where the deflection distance at the center of the surface is 4 mm. This deformation restricts the aperture diameter in which four water reflections are encountered. For off-normal or off-center rays, deflection of the second surface can direct rays entirely out of the desired path. If the off-normal rays were incident at an angle larger than 6° as shown in Fig. 6, the fourth reflection would not occur, or the rays would not exit the entrance aperture despite encountering four water reflections. This can significantly hinder reflectivity measurements, as a slight misalignment (in either angle or position) of the source leads to a displaced reflection. Additionally, the ray triplets are diffused by an amount based on the curvature of the deflected surface; for example, for 4 mm deflection, the off-normal rays exit the aperture at twice their initial separation distance.

One last effect must be considered: in the millimeter-wave/terahertz frequency range, atmospheric attenuation at sea level with 100% humidity increases from 0.002 dB/m at $f = 100$ GHz to 0.2 dB/m just above $f = 1$ THz [35]. Table 1 shows the frequency ranges where the attenuation through the effective path length in the ABC source (0.5 m) is greater than 2% at sea level, with 50% relative humidity, at 295 K. We emphasize that the ABC source is intended for indoor laboratory use, where 50% relative humidity is a reasonable upper limit. If a broadband detector is used, its frequency response needs to be calibrated to account for the absorption bands in Table 1. Pressure and humidity should be estimated for the specific location where the ABC source is used, and radiometric temperature corrected for the environment.

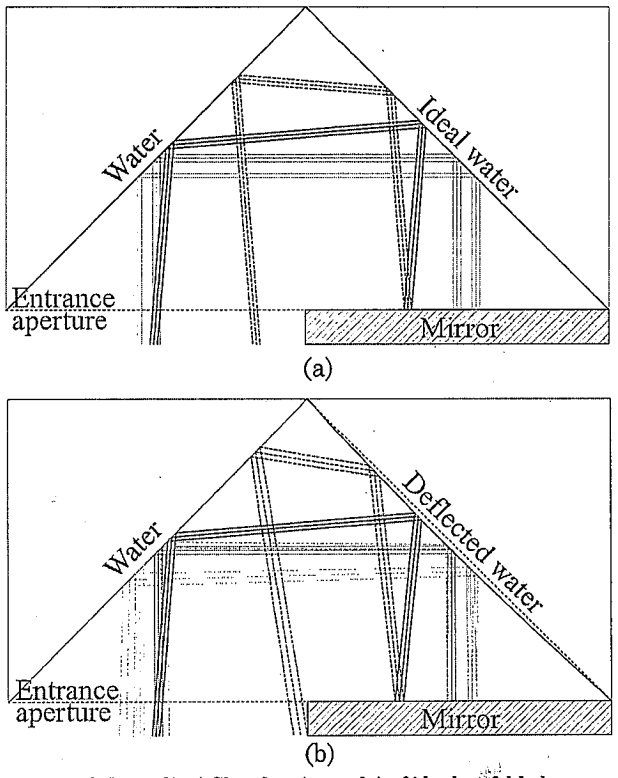

Fig. 6. (Color online) Sketches (to scale) of ideal unfolded geometry (a) and nonideal geometry with convex second reflection surface (b). The red (online) rays are the central rays, the blue rays are centered in the entrance aperture but rotated 5° from normal, and the green rays are normal to the aperture but offset from the center by 2.5 cm. The deflection at the center of the nonideal curved surface is 4 mm from the ideal flat surface. It is clear that the rays entering the aperture at the off-normal angle are affected the most by the deflected water surface. Note that besides the obvious translation for the off-center and off-normal incident rays, the ray triplets upon exiting are twice their initial separation.

Table 1. Atmospheric Bands Below $f = 1$ THz Where Attenuation Exceeds 2% [a]

f_{start} (GHz)	f_{peak} (GHz)	f_{end} (GHz)	Peak Attenuation (dB)
376.8	380.2	383.7	0.1856
444.0	448.0	451.8	0.2211
520.6	557.0	600.1	10.45
615.5	620.7	624.9	0.1957
720.3	752.0	787.0	7.245
909.5	916.2	923.2	0.3717
955.4	—	—	—

[a]Calculated for atmospheric conditions of $T = 295$ K, 101.325 kPa (mean sea-level pressure), and 50% relative humidity. Distance is 0.5 m, the mean path length in the ABC source. For the band beginning at $f = 955.4$ GHz, attenuation does not drop below 2% before $f = 1$ THz, indicated by the "—" dashes.

We restate that the nonidealities discussed in this subsection are included for completeness but do not appear in the uncertainty budget because they do not affect T_r under normal operating conditions.

G. Summary of Radiometric Accuracy

The radiometric temperature T_r at the entrance aperture of the ABC source can be calculated, under certain assumptions, from radiative transfer as described in Appendix A. The radiometric temperature error is plotted versus frequency in Fig. 7, where T_r is obtained from Eq. (A1). As mentioned above, performance at low frequencies is reduced primarily by R_w and is a calculable correction, and at high frequencies primarily by A_e, and is an uncertainty. To generate Fig. 7, the frequency dependence of R_w was taken from the calculations based on Kindt and Schmuttenmaer [26] and Rønne *et al.* [31] (displayed in Fig. 5), and the error bars below $f = 250$ GHz are deduced from their uncertainty reported in the double-Debye model parameters. The frequency dependence of A_e was obtained by fitting the measurements described in Subsection 3.C and Fig. 4 to the form $y = 1/2\{1 + \mathrm{erf}[(x-\mu)/(\sigma\sqrt{2})]\}$ and is responsible for the error bars above $f = 300$ GHz. Mirror absorbance as a function of frequency was set to Eq. (1). The uncertainty in T_w is not shown in this plot in order to emphasize the roles of uncertainty from R_w and A_e. The plotted quantity is $T_r - T_w$, the error in the measured quantity. For example, if a measurement is performed at $f = 200$ GHz with a desired signal of $T_w - T_0 = 40$ K, a calibrated radiometer will measure a signal of 39.6 K. Adding the correction of 0.4 K [as per Eq. (A1) and Fig. 7] eliminates the measurement error; the combined uncertainty at $f = 200$ GHz in the parameters of Eq. (A1) is approximately ±0.40 K, using the root-sum-square method.

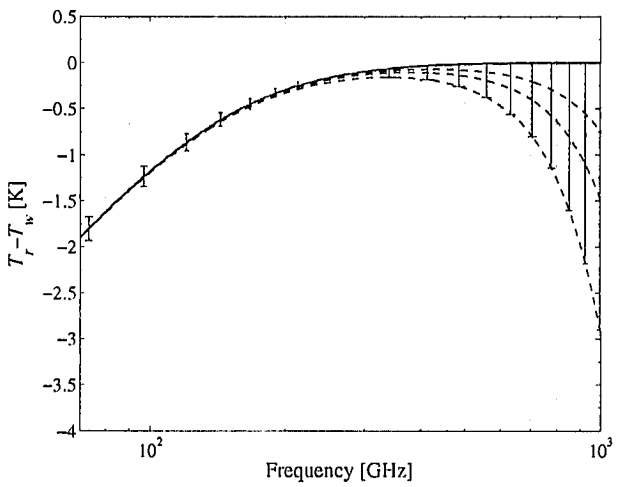

Fig. 7. (Color online) Radiometric temperature correction (thick solid line) as a function of frequency for a common signal strength of $T_w - T_0 = 40$ K, where $T_w = 333$ K. The error bars below $f = 250$ GHz are obtained from the reported uncertainty in the double-Debye water model fit parameters from [26,31], and the error bars above $f = 300$ GHz are due to the unknown balance between absorption and scattering in the EPS. The dashed lines indicate the corrections that would occur, rather than uncertainty, if A_e were known to be 25%, 50%, or 100% absorption, from top to bottom.

Table 2 summarizes the uncertainty analysis at two frequencies, $f = 100$ GHz and $f = 500$ GHz. At the W-band, the radiometric temperature correction for the ABC source is +1.5 K for a 40 K signal ($T_w = 333$ K), and the combined uncertainty (root-sum-square method) is ±0.40 K. The thermometry uncertainty accounts for ±0.23 K, and uncertainties in R_w (shown in Fig. 7), A_e, and A_m, account for the remainder. At $f = 500$ GHz, the correction is +30 mK, and the combined uncertainty is ±0.37 K.

The effects of scattering, roughness, EPS deflection, diffraction, and atmospheric absorption are shown in Table 3. Rather than adding uncertainty or an additional correction, they limit the range over which the radiometric temperature accuracy is valid. Based on the previous discussion, scattering and roughness are negligible at lower frequencies. Correction due to atmospheric attenuation contributes only in the noted frequency ranges (Table 1), where its value is significantly comparable to the other uncertainties. Scattering at high frequencies and EPS deflection limit the area and solid angle to a smaller range in area and solid angle than the nominal range indicated in Fig. 3. Reduction of radiative transfer and/or $A\Omega$ due to diffraction is calculable [32,33], or avoidable with use of the proper measurement geometry.

4. Reflectivity Measurements

An estimate of the effective emissivity of the ABC source can be obtained by measuring the reflected power of a source that is directed into the entrance aperture. Because of the absorbance of liquid water, the effective emissivity will equal (1 – reflectance) when all reflected power is measured. This reflectance is measured by spatially integrating the reflected power when the container is filled with water and then dividing by the integrated reflected power when mirrors replace the water surfaces. This is a valid approach as long as the entire reflected beam is contained in the mapped region. Integrated reflected power measured with mirrors in place of water is corrected for imperfect mirror reflectance.

To validate the ABC source design, a set of reflectance measurements was performed in the range of $f = (80–260)$ GHz, where sources and detectors were readily available. Although limited, these measurements verify predicted water reflectance at the measured frequencies, justifying confidence throughout the band. For reflectance measurements, the incident beam from a horn antenna located in one half of the entrance aperture is directed such that the reflection is in the other half of the entrance aperture. In some cases, PTFE lenses are used to collimate the incident beam. Figure 8 contains examples of measured reflectance maps with mirrors (top) and water (bottom) for a collimated $f = 105$ GHz incident beam.

Table 2. Uncertainty Budget: Uncertainty in T_r Due to Uncertainties in Parameters of Eq. (A1) for $T_w = 333\,K$ and $T_0 = 293\,K$

	$f = 100\,GHz$		$f = 500\,GHz$	
	Value	Uncertainty (K)	Value	Uncertainty (K)
Water temperature T_w (K)	333.0 ± 0.24	± 0.23	333.0 ± 0.24	± 0.24
EPS absorbance A_e	0 ± 0.007	± 0.27	$0 + 0.02$	± 0.28
Mirror absorbance A_m	$0 + 0.05$	± 0.15	$0 + 0.05$	± 0.03
Water reflectance R_w	0.432 ± 0.009	± 0.12	0.167 ± 0.011	± 0.01
Combined uncertainty (K)		± 0.40		± 0.37

The reflection from the water surfaces is spatially shifted *and* diffused, corresponding to the geometry illustrated by Fig. 6 due to the curvature of the second EPS–water interface. Table 4 summarizes the measured reflectance at several frequencies in the W-band and at $f = 260\,GHz$. All measurements lie within the corrections predicted from Appendix A. Radiometric accuracy implied by these measurements is within the uncertainty of the value $(1 - R_{ws}^4 R_{wp}^2)$. This is not surprising, given that the uncertainty in the lower half of the frequency range is not dominated by the uncertainty from EPS. These results provide confidence in the correction for the residual reflectance due to water, Eq. (A5).

5. Conclusion

In summary, this paper presents the first calibrated broadband blackbody source developed as part of a new metrology infrastructure for the millimeter-wave/terahertz frequency range. The ABC source is easy to fabricate, inexpensive to manufacture and operate, reproducible, scalable, and easily adaptable to a variety of measurement scenarios. Uncertainty from the W-band to $f = 450\,GHz$ is no less than $\pm 0.24\,K$, due to the accuracy of the thermometry, and also depends on the published uncertainty in the complex refractive index of water. Above $f = 450\,GHz$, uncertainty is dominated by the unknown balance between absorption and scattering in the EPS. If the balance were better known, a correction would be applied, and uncertainty would be reduced. The measured reflectance results agree with the predicted values up to the highest measured frequency, $f = 260\,GHz$. In the future, validation will be extended to higher frequencies with a new set of sources and detectors, and the balance between absorption and scattering in EPS will be examined.

Table 3. Other Effects

Category	Effect	Remedy
Atmospheric transmission	Radiative transfer reduction	Calculate; see Table 1
EPS deflection	Reduction of $A\Omega$	Ensure $\theta_{xy} < 6°$
Spatial nonuniformity of T_w	Introduces a minimum time between ΔT_w and radiometric measurement	Wait 1 min
Water surface scattering	Reduction of $A\Omega$	Calculate; see [32]
Diffraction	Geometry-dependent reduction of $A\Omega$	Calculate; see [33,34]

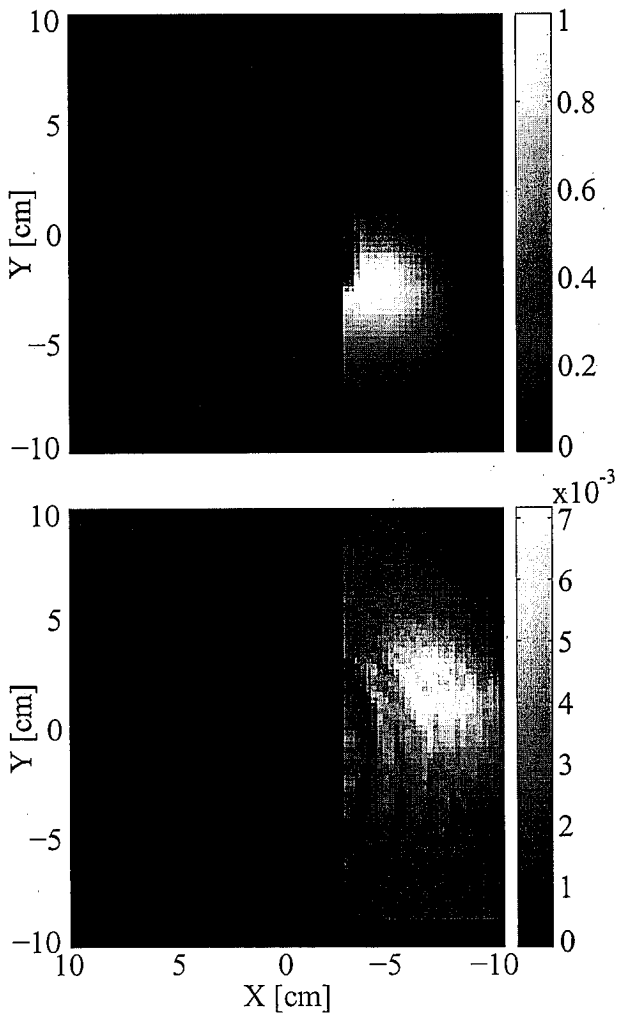

Fig. 8. Measured reflectance maps for mirror surfaces (top) and water surface (bottom). The maps are scaled to fit the size of the entrance aperture; the source and focusing lenses block the leftmost 12 cm of the entrance aperture, with the nominal specular reflection in the rightmost 8 cm (the mappable region). Lens shadow can be seen (top), as well as the distorted and displaced beam (bottom) due to the curved water surface (Fig. 6).

Table 4. Summary of Reflectance Measurements

Frequency (GHz)	Reflected Power (%)
83	1.21
105	0.75
105 (w/lens)	1.45
260	<0.15[a]

[a]At $f = 260$ GHz, measured reflection maps from water surfaces were indistinguishable (within 95% confidence intervals when fitted to a Rayleigh or Gaussian distribution) from reflection maps taken with the source blocked; 0.15% is a statistical upper bound.

Appendix A

In contrast to many infrared blackbodies, the geometry of the ABC source is simple enough that the effects of the secondary dependencies of T_r on other parameters—for example, EPS loss—can be analytically calculated. These calculations are outlined here. The assumptions made are as follows:

1. Transmission through the water behind each EPS–water interface is zero. Therefore, $R_w + A_w = 1$.
2. Transmission through the mirror is zero. Therefore, $R_m + A_m = 1$.
3. Reflectance off each air–EPS interface is zero. Therefore, $\tau_e + A_e = 1$. This is valid because the EPS refractive index, n_{EPS}, is close to unity [29]. We further assume that the single-pass EPS absorbance is small ($A_e \ll 1$) so that for a multipass situation, $(1 - A_e)^p = (1 - pA_e)$, where p is the number of passes.
4. Volume scattering within the EPS is negligible, and surface scattering (diffuse reflection) at the EPS–water interfaces is also negligible. This is discussed in the main text.
5. Coherent effects, particularly coherent interference between multiple reflections, can be neglected. This is reasonable given that the ABC source is intended as an emitter of *broadband* radiation; over a sufficiently broad bandwidth, coherent interference (standing waves) is blurred beyond discrimination. This minimum bandwidth is the free spectral range of the shortest cavity formed within the system. The smallest dimension is the wall thickness, $t = 1$ cm; this yields a free spectral range of $c/2n_{\mathrm{EPS}}t = 15$ GHz.

Neglecting coherence, the analysis of radiative transfer through the ABC source is greatly simplified. The radiometric temperature at plane $(i-1)$, $T_r^{(i-1)}$, is transformed into a radiometric temperature at plane (i), $T_r^{(i)}$, according to

$$T_r^{(i)} = (1 - A_e)T_r^{(i-1)} + A_e T_e \quad \text{for transmission through an EPS layer at temperature } T_e,$$

$$T_r^{(i)} = R_{w(s,p)}^{(i-1)} + (1 - R_{w(s,p)})T_w \quad \text{for } s(p) \text{ reflection off an EPS-water interface, and}$$

$$T_r^{(i)} = R_m T_r^{(i-1)} + (1 - R_m)T_m \quad \text{for reflection off an imperfect mirror at temperature } T_m.$$

Based on the above assumptions, the radiometric temperature at the entrance aperture is given in terms of the water, EPS, mirror, and ambient temperatures by

$$\begin{aligned} T_{rV} = {} & T_{wV}(1 - A_e)\Big[(1 - R_{ws}) + (1 - R_{wp})R_{ws}(1 - A_e)^2 \\ & + (1 - R_{wp})R_{wp}R_{ws}R_m(1 - A_e)^4 \\ & + (1 - R_{ws})R_{wp}^2R_{ws}R_m(1 - A_e)^6\Big] \\ & + T_{eV}A_e\Big\{1 + R_{ws}[(1 - A_e) + (1 - A_e)^2] \\ & + R_{wp}R_{ws}(1 - A_e)^3 + R_{wp}R_{ws}R_m(1 - A_e)^4 \\ & + R_{wp}^2R_{ws}R_m[(1 - A_e)^5 + (1 - A_e)^6] \\ & + R_{wp}^2R_{ws}^2R_m(1 - A_e)^7\Big\} \\ & + T_{mV}A_mR_{ws}R_{wp}(1 - A_e)^4 \\ & + T_{0V}R_{wp}^2R_{ws}^2R_m(1 - A_e)^8. \end{aligned} \tag{A1}$$

In the above equation, T_{rV} is the radiometric temperature for the polarization where the electric field is vertical in the entrance aperture. For V polarization, the sequence of reflections is s, p, p, s, and for H polarization it is p, s, s, p. Thus the analogous expression for T_{rH} is obtained by interchanging s and p in Eq. (A1). While A_e and A_m are polarization independent, the water reflectance $R_{w(s,p)}$ is polarization dependent.

Equation (A1) enables us to estimate the systematic uncertainties or corrections in radiometric temperature due to nonideal materials. A known deviation of A_e, A_m, or R_w from zero produces a calculable correction in T_r, and an uncertainty in A_e, A_m, or R_w produces an uncertainty in T_r that is calculable through the law of propagation of uncertainty [26]. We evaluate these uncertainties quantitatively, using our best estimates for A_e, A_m, and R_w, and their frequency dependence. The general formulas are given below, while the numerical values for various uncertainties at two particular frequencies ($f = 100$ GHz and $f = 500$ GHz) at a signal strength of ($T_w - T_0 = 40$ K) are summarized in Table 2. We use the facts that the mirror temperature is ambient and the effective EPS temperature is the mean between the water and ambient temperatures, that is, $T_m = T_0$ and $T_e = (T_w + T_0)/2$, and $(1 - A_e)^p = (1 - pA_e)$ to simplify Eq. (A1), yielding

$$T_{rV} = T_{wV}(1-A_e)\Big[(1-R_{ws}) + (1-R_{wp})R_{ws}(1-2A_e) + \left(\frac{T_{wV}+T_{0V}}{2}\right)[1+R_{ws}(2-3A_e) + R_{wp}R_{ws}(1-3A_e) + R_mR_{wp}R_{ws}(1-4A_e) + R_mR_{wp}^2R_{ws}(2-11A_e) + R_mR_{ws}^2R_{wp}^2(1-7A_e)\Big] + T_{0V}A_mR_{ws}R_{wp}(1-4A_e) + T_{0V}R_{wp}^2R_{ws}^2R_m(1-8A_e). \quad \text{(A2)}$$

The idea is to expand the radiometric error in T_r from Eq. (A2) by a Taylor expansion about the nominal values of A_e, R_w, A_m, and T_w. The corrections and uncertainties due to A_e, A_m, and R_w are all proportional to signal strength in an actual measurement, because the difference between T_r and T_0 is the measured quantity. The uncertainty in T_r due to the unknown balance between EPS scattering and absorption, embodied by the term A_e, is given by

$$\left|\frac{\partial T_{rV}}{\partial A_e}\right|\Delta A_e = \Delta A_e\Big[-T_{0V}R_{ws}(3+7R_{wp}+11R_{wp}^2 + 23R_{wp}^2R_{ws})/2 - T_{ws}(2+7R_{wV}-8A_eR_{ws} + 11R_{wp}R_{ws} - 8A_eR_{wp}R_{ws} + 15R_{wp}^2R_{ws} - 8A_eR_{wp}^2R_{ws} - 7R_{wp}^2R_{ws}^2 + 24A_eR_{wp}^2R_{ws}^2)/2\Big], \quad \text{(A3)}$$

where ΔA_e is the uncertainty in A_e. At $f = 100$ GHz, $\Delta A_e < 0.005 \times \sqrt{2} = 0.0071$, and at high frequencies from the measurements shown in Fig. 4. In the case of $A_e = 0$, we are assigning all loss to scattering, rather than absorption. The correction in T_r due to the calculable mirror absorption A_m is obtained by setting A_m equal to the complement of Eq. (1). This is negligible compared to other corrections and uncertainties. The uncertainty is given by

$$\left|\frac{\partial T_{rV}}{\partial A_m}\right|\Delta A_m = \Delta A_m\Big[T_{ws}R_{wp}R_{ws}(-3-2R_{wp}+R_{wp}R_{ws})/2 - T_{0s}R_{wp}R_{ws}(-1+2R_{wp}+3R_{wp}R_{ws})/2\Big]. \quad \text{(A4)}$$

At both $f = 100$ GHz and $f = 500$ GHz we set A_m to 0.05, as mentioned in the prior discussions. Next, we address the finite reflectance of water. The value

$$T_r - T_w = -R_{ws}^2R_{wp}^2(T_w - T_0) \quad \text{(A5)}$$

is a calculable correction for the finite return loss of the ABC source, due to the nonzero reflectivity of water. The uncertainty in this correction is determined by the uncertainty in R_w, which results from the uncertainty in the complex refractive index measurements of water by Kindt and Schmuttenmaer [26] and Rønne *et al.* [31]. The uncertainty in (A1) due to the uncertainty in R_w is therefore given by

$$\left|\frac{\partial T_{rV}}{\partial R_{ws}}\right|\Delta R_w = \Delta R_w\Big[T_{0s}(1+R_{wp}+R_{wp}^2+3R_{wp}^2R_{ws}) - T_{ws}(-1-R_{wp}-R_{wp}^2+R_{wp}^2R_{ws})\Big], \quad \text{(A6)}$$

keeping in mind that the same derivative with respect to R_{wp} is required as well. Finally, we examine the effect of uncertainty in T_w, given by

$$\left|\frac{\partial T_{rV}}{\partial T_{wV}}\right|\Delta T_w = \Delta T_w(3/2+R_{ws}+R_{wp}R_{ws}+R_{wp}^2R_{ws} - R_{wp}^2R_{ws}^2/2), \quad \text{(A7)}$$

which shows that for an uncertainty in T_w (the Type B uncertainty in the thermometry), the resulting uncertainty in T_r is essentially the same.

The authors thank Christopher Cromer for useful comments during the preparation of this manuscript, John Lehman for suggestions during the initial design, and the Defense Advanced Research Projects Agency Microantenna Arrays: Microsystems Technology (DARPA MIATA) Office program for providing the motivation for this work. C. Dietlein thanks the National Science Foundation (NSF) for funding under grant #0501578.

References

1. D. W. Woolard, E. R. Brown, M. Pepper, and M. Kemp, "Terahertz frequency sensing and imaging: a time of reckoning future applications?," Proc. IEEE **93**, 1722–1743 (2005).
2. P. H. Siegel, "Terahertz technology," IEEE Trans. Microwave Theory Tech. **50**, 910–928 (2002).
3. P. H. Siegel, "Terahertz technology in biology and medicine," IEEE Trans. Microwave Theory Tech. **52**, 2438–2447 (2004).
4. J. Randa, D. K. Walker, A. E. Cox, and R. L. Billinger, "Errors resulting from reflectivity of calibration targets," IEEE Trans. Geosci. Remote Sens. **43**, 50–58 (2005).
5. K. Foster and T. Hewison, "The absolute calibration of total power millimeter-wave airborne radiometers," in *Proceedings of the 1998 IEEE International Geoscience and Remote Sensing Symposium* (IEEE, 1998), pp. 384–386.
6. C. M. Stickley and M. Filipkowski, "MIcroantenna Arrays: Technology and Applications (MIATA)–an overview," Proc. SPIE **5619**, 47–58 (2004).
7. J. A. Shaw and L. S. Fedor, "Improved calibration of infrared radiometers for cloud temperature remote sensing," Opt. Eng. **32**, 1002–1010 (1993).
8. I. M. Mason, P. H. Sheather, J. A. Bowles, and G. Davies, "Blackbody calibration sources of high accuracy for a spaceborne infrared instrument: the Along Track Scanning Radiometer," Appl. Opt. **35**, 629–639 (1996).
9. A. C. Parr, "A national measurement system for radiometry, photometry, and pyrometry based upon absolute detectors," http://physics.nist.gov/Pubs/TN1421/contents.html.
10. H. W. Yoon, C. E. Gibson, and P. Y. Barnes., "The realization of the NIST detector-based spectral irradiance scale," Metrologia **40**, S172 (2003).

11. G. T. Fraser, C. E. Gibson, H. W. Yoon, and A. C. Parr, ""Once is enough" in radiometric calibrations," J. Res. Natl. Inst. Stand. Technol. **112**, 39–51 (2007).
12. F. Hengstberger, *Absolute Radiometry* (Academic, 1989).
13. E. N. Grossman, C. Dietlein, and A. Luukanen, "Terahertz circular variable filters," in *Proceedings of the 4th ESA Workshop on Millimetre-wave Technology and Applications* (European Space Agency, 2006), pp. 353–358 .
14. M. E. MacDonald, A. Alexanian, R. A. York, Z. Popović, and E. N. Grossman, "Spectral transmittance of lossy printed resonant-grid terahertz bandpass filters," IEEE Trans. Microwave Theory Tech. **48**, 712–718 (2000).
15. D. W. Porterfield, J. L. Hesler, R. Densing, E. R. Mueller, T. W. Crowe, and R. M. Weikle II, "Resonant metal mesh bandpass filters for the far-infrared," Appl. Opt. **33**, 6046–6052 (1994).
16. R. H. Giles and T. M. Horgan, "Method for absorbing radiation," U.S. patent 5,260,513 (9 November, 1993).
17. P. F. Goldsmith, R. A. Kot, and R. T. Iwasaki, "Microwave radiometer blackbody calibration standard for use at millimeter wavelengths," Rev. Sci. Instrum. **50**, 1120–1122 (1979).
18. P. H. Siegel, R. H. Tuffias, and P. Goy, "A simple millimeter-wave blackbody load," in *Proceedings of the 9th International Conference on Space THz Technology* (Jet Propulsion Laboratory, 1998), pp. 1–10.
19. A. E. Cox, J. J. O'Connell, and J. Rice, "Initial results from the infrared calibration and infrared imaging of a microwave calibration target," in *Proceedings of the 2006 IEEE Geoscience and Remote Sensing Symposium* (IEEE, 2006), 3463–3465.
20. J. B. Fowler, "A third generation water bath based blackbody source," J. Res. Natl. Inst. Stand. Technol. **100**, 591–599 (1995).
21. E. F. Zalewski and C. R. Duda, "Silicon photodiode device with 100% external quantum efficiency," Appl. Opt. **22**, 2867–2873 (1983).
22. N. P. Fox, "Trap detectors and their properties," Metrologia **28**, 197–202 (1991).
23. J. L. Gardner, "Transmission trap detectors," Appl. Opt. **33**, 5914–5918 (1994).
24. J. H. Lehman and C. L. Cromer, "Optical trap detector for calibration of optical fiber powermeters: coupling efficiency," Appl. Opt. **41**, 6531–6536 (2002).
25. J. H. Lehman and C. L. Cromer, "Optical tunnel-trap detector for radiometric measurements," Metrologia **37**, 477–480 (2000).
26. J. T. Kindt and C. A. Schmuttenmaer, "Far-infrared dielectric properties of polar liquids probed by femtosecond terahertz pulse spectroscopy," J. Phys. Chem. **100**, 10373–10379 (1996).
27. B. N. Taylor and C. E. Kuyatt, "Guidelines for evaluating and expressing the uncertainty of NIST measurement results," NIST Tech. Note 1297 (NIST, 1994).
28. Central Bureau of the International Electrotechnical Commission, "Industrial platinum resistance thermometer sensors," International Electrotechnical Commission (IEC) Publ. 751 (IEC,1996).
29. G. Zhao, M. ter Mors, T. Wenckebach, and P. C. M. Planken, "Terahertz dielectric properties of polystyrene foam," J. Opt. Soc. Am. B **19**, 1476–1479 (2002).
30. J. Xu, K. W. Plaxco, S. J. Allen, J. E. Bjarnason, and E. R. Brown, "0.15–3.72 THz absorption of aqueous salts and saline solutions," Appl. Phys. Lett. **90**, 1–3 (2007).
31. C. Rønne, L. Thrane, P.-O. Astrand, A. Wallqvist, K. V. Mikkelsen, and S. R. Keiding, "Investigation of the temperature dependence of dielectric relaxation in liquid water by THz reflection spectroscopy and molecular dynamics simulation," J. Chem. Phys. **107**, 5319–5331 (1997).
32. J. M. Bennett and L. Mattsson, *Introduction to Surface Roughness and Scattering* (Optical Society of America, 1989).
33. E. L. Shirley, "Revised formulas for diffraction effects with point and extended sources," Appl. Opt. **37**, 6581–6590 (1998).
34. E. L. Shirley, "Fraunhofer diffraction effects on total power for a Planckian source," J. Res. Natl. Inst. Stand. Technol. **106**, 775–779 (2001).
35. H. B. Wallace, "AEM" software.